Received: 8 March 2019 | Revised: 22 July 2019 | Accepted: 22 July 2019

DOI: 10.1111/jace.16716

Journal of the American Ceramic Society

INVITED FEATURE ARTICLE

Analyzing the grain-boundary resistance of oxide-ion conducting electrolytes: Poisson-Cahn vs Poisson-Boltzmann theories

Xiaorui Tong[1] | **David S. Mebane**[1] | **Roger A. De Souza**[2]

[1]Department of Mechanical and Aerospace Engineering, West Virginia University, Morgantown, WV, USA

[2]Institute of Physical Chemistry, RWTH Aachen University, Aachen, Germany

Correspondence
Roger A. De Souza, Institute of Physical Chemistry, RWTH Aachen University, 52056 Aachen, Germany.
Email: desouza@pc.rwth-aachen.de

Funding information
National Science Foundation, Grant/Award Number: CBET-1705397; German Research Foundation, Grant/Award Number: SO 499/9-1

Abstract

The diminished conductivity of pristine grain boundaries in oxide-ion conducting electrolytes, such as $(Ce,Gd)O_2$ and $(Zr,Y)O_2$, is widely interpreted with the Mott-Schottky space-charge model, or less frequently, with the Gouy-Chapman space-charge model. Although routinely applied to the entire compositional range of solid solutions, from dilute to concentrated, these models, being based on the Poisson-Boltzmann formalism, are limited in their range of validity to dilute solutions of point defects. Analyzing the grain-boundary properties of concentrated solid solutions with such models is expected to lead to errors and inconsistencies. In this study, we employ Poisson-Cahn theory to analyze literature data for the grain-boundary resistance of CeO_2-Gd_2O_3 materials as a function of Gd concentration. Poisson-Cahn theory combines the Cahn-Hilliard theory of inhomogeneous systems with the Poisson equation of electrostatics and it is valid over the entire compositional range. We treat the realistic case of a restricted equilibrium: Gd accumulation profiles are frozen-in from sintering temperatures, while the oxygen-vacancy distributions are in equilibrium at sintering and (much lower) measurement temperatures. Data for the grain-boundary resistance are also analyzed with the standard analytical expressions from the Mott-Schottky and Gouy-Chapman models. Outside the domain of their validity, these expressions are found to perform poorly. In general, we emphasize the importance of treating the interfacial properties of concentrated solid solutions with physically appropriate theories.

1 | INTRODUCTION

The electrical response of a crystalline oxide is often governed by interactions between the system's point defects and its interfaces. The segregation of charged point-defects to a grain boundary, for instance, results in the grain boundary becoming electrostatically charged and space-charge zones forming in the adjacent bulk phase to preserve global electroneutrality. This re-distribution of charged point-defects may alter local point-defect concentrations in the vicinity of a boundary by many orders of magnitude, and thus, it may give rise to grain boundaries that are, relative to the bulk phase, highly conductive or highly resistive.

The abrupt core|space-charge model[1–8] currently represents the standard treatment of space-charge layers at grain boundaries in complex oxides. It is essentially a two-phase model, in which a grain-boundary core phase is sandwiched between two slabs of bulk material, the grain-boundary core being the structurally perturbed region between the two grains. (Since the grain-boundary core is characterized by a finite width and by a distinct set of thermodynamic quantities, and since it is in (partial)

thermodynamic equilibrium with the adjacent slabs of bulk phase but cannot exist independently of them, it can be termed a grain-boundary complexion[9,10].) The usefulness of the abrupt corelspace-charge model is that it easily links observable physical properties, such as the grain boundaries' resistance and capacitance, to space-charge quantities such as the space-charge potential, which describes the degree to which point defects are depleted or accumulated in the space-charge zone, and the space-charge screening length, which describes the length scale over which such changes occur.

For systems that contain a dopant and one charge-compensating defect, two limiting cases are commonly considered in the literature: (a) the Gouy-Chapman case, in which both dopant and charge-compensating defect are mobile and their concentration profiles are in electrochemical equilibrium; (b) the Mott-Schottky case, in which the dopant's concentration is constant across the entire system, and only the mobile compensating defect is in electrochemical equilibrium. (These two limiting cases are considered because they lead to simple analytical expressions linking space-charge parameters to observable properties.) Many actual samples, however, will be characterized by some intermediate case, one in which the exact concentration profile of the dopant conforms neither to the Mott-Schottky nor to the Gouy-Chapman case. Such intermediate cases result whenever the dopant is mobile at fabrication temperatures (ie, sintering and conditioning of the polycrystalline oxide) but not at the (much lower) temperatures at which electrical measurements are made (ie, at those temperatures at which the space-charge layers are probed). The critical factors, therefore, are the thermal history of the sample and the mobility of the dopant.

One oxide system whose grain boundaries have received much attention is the fluorite-structured oxide CeO_2.[5,11–45] The total ionic conductivity of the solid solutions CeO_2-M_2O_3 is sufficiently high that the materials find application as oxygen-ion conducting electrolytes in intermediate temperature solid oxide fuel cells,[46–52] despite pristine grain boundaries exhibiting substantially lower conductivity than the bulk phase. Since the structural perturbation on its own is deemed insufficient to generate such considerable resistance, and since the grain-boundary width extracted from capacitance measurements is much larger than the structurally perturbed (core) region observed in transmission electron micrographs, it has been concluded that the high resistance is due to diffuse space-charge layers depleted of oxygen vacancies.

The formation of space-charge layers at grain boundaries in CeO_2-based materials is widely attributed to the behavior of ionic defects (as opposed to the trapping of electronic defects in interface states). Specifically, oxygen vacancies, in response to their Gibbs formation energy being lower at the core than in the bulk,[2,5,7,53] segregate from bulk to core. The grain-boundary core thus develops an excess positive charge, and this charge is compensated by negatively charged space-charge zones, in which, at least in the dilute-solution picture, oxygen vacancies are strongly depleted and acceptor-dopant cations, if sufficiently mobile, are accumulated.

It is worth taking note of our use of the terms "segregation" and "accumulation." Following Ref. [7], we use "segregation" to refer to the redistribution of a defect from the bulk to the core, increasing the concentration of that defect in the core; and we use "accumulation" to refer to the redistribution from bulk to the diffuse space-charge layers, increasing the concentration of that defect within the layers. Defect segregation does not necessarily imply defect accumulation, and vice versa.

Grain-boundary resistances measured for CeO_2-M_2O_3 solid solutions at $T < 1000$ K are generally analyzed[24,31,34,35,40,54–59] within the Mott-Schottky approach (with one notable exception[5]). Such an analysis ignores, however, two things. First, that concentrated solid solutions are being studied, whereas Mott-Schottky (and Gouy-Chapman) approaches, being based on the Poisson-Boltzmann formulism, are only valid for dilute solutions. Second, that dopant accumulation will have occurred at sintering temperatures. Atomic-level characterization by means of transmission electron microscopy[38,60–64] (TEM) or atom probe tomography (APT)[65,66] has found significant accumulation of the acceptor cation at grain boundaries in CeO_2 solid solutions (grain boundaries in the related ZrO_2-Y_2O_3 materials also show accumulation of the Y cations[60,67–70]). Acceptor-cation accumulation can only take place at sintering temperatures because cation transport in fluorite-structured oxides, such as CeO_2 and ZrO_2, is extremely slow (orders of magnitude slower than oxygen transport) and because it is characterized by much higher activation energies.[71–75] Knowledge of a sample's thermal history is thus essential to the interpretation of experimental results.

In this study, we analyze the grain-boundary resistance of CeO_2-Gd_2O_3 materials, moving beyond these usual assumptions of no dopant accumulation and of a dilute solution. To this end, we extend our previous work on space-charge layers at grain boundaries in the theoretical framework of Poisson-Cahn theory.[76] Combining Poisson-Boltzmann and Cahn-Hilliard[77,78] formalisms, Poisson-Cahn theory[76,79,80] is able to treat space-charge layers at extended defects over the entire compositional space, from weakly doped systems up to concentrated solid solutions. We extend our previous study in one particular way: We take into account the (temperature-dependent) mobility of the cations and the thermal history of the sample. That is, we consider the realistic case of a restricted equilibrium in which (a) oxygen ions achieve electrochemical equilibrium quasi-instantaneously at all temperatures; and (b) the Gd^{3+} cations are allowed to attain electrochemical equilibrium at elevated (sintering) temperature, reacting to the electric potential profile set up by the vacancies' redistribution, but are frozen-in at lower, measuring temperatures. We

also extend the work of Tschöpe et al,[5] who did consider such a restricted equilibrium but only within the framework of a dilute solution. Finally, we also provide a detailed comparison of Poisson-Cahn theory with its dilute-solution cousins.

Our study is set out as follows. The following section summarises the standard dilute-solution approaches, providing a foundation for the rest of the paper. Poisson-Cahn theory is described in detail in the third section; the derivation of a characteristic length is also discussed. In the fourth section, results are presented; conductivity data from the literature are also analyzed with Poisson-Cahn theory and with the standard Poisson-Boltzmann theories.

2 | THE STANDARD POISSON-BOLTZMANN TREATMENTS

The principal aim of the standard treatments is to obtain simple analytical expressions for the grain-boundary resistance R^{gb} in terms of space-charge potential Φ_0. We reproduce below the major equations, although they have been reported elsewhere,[18,81–83] so that the assumptions involved in deriving such expressions are evident, and in this way, the conditions under which the expressions are valid are clear. This information is required later (Section 4.3), when experimental data are analyzed with Poisson-Cahn theory and with the standard approaches, and comparisons are made. Some mistakes and misconceptions in published studies are also cleared up.

Our considerations are restricted to an AO_2 oxide containing acceptor cations (site fraction n_a) and charge-compensating oxygen vacancies (site fraction n_v). Electrons are neglected on the assumption that they are minority species in the bulk and in the space-charge layers; this is a reasonable approximation for a CeO_2-M_2O_3 material under oxidizing conditions and at not too high temperatures.[74] In the bulk, the electroneutrality condition is thus $n_a^b = 4n_v^b$ (since the concentrations are related through $c_a^b = 2c_v^b$ and the site densities in an AO_2 oxide through $2N_a^b = N_v^b$).

The standard treatments of Gouy-Chapman and Mott-Schottky space-charge layers in ionic solids are based on two main assumptions. First, materials' parameters, such as charge-carrier mobilities or standard chemical potentials, are assumed to exhibit step functions at the core (abrupt core|space-charge model[3,4,7]). That is, the mobilities, for example, exhibit one value in the bulk phase all the way up to the core and a different value in the grain-boundary core. Second, point defects are assumed to behave as dilute, non-interacting defects. The electrochemical potentials of the two defects (as building units) in the bulk and in the core take, therefore, the standard Maxwell-Boltzmann form,[7,84,85]

$$\tilde{\mu}_v = \mu_v^{\ominus} + k_B T \ln n_v + 2e\phi \tag{1a}$$

$$\tilde{\mu}_a = \mu_a^{\ominus} + k_B T \ln n_a - e\phi. \tag{1b}$$

where $\mu^{\ominus}$ are the standard chemical potentials of the defect building units; ϕ is the electric potential; and k_B, T, and e have their usual meanings. It is the difference in $\mu_v^{\ominus}$ between bulk phase and core phase, with $\mu_v^{\ominus,c} - \mu_v^{\ominus,b} < 0$, that drives the formation of the space-charge layers in our AO_2 oxide.[5,7]

A defect (building unit) is considered to be in electrochemical equilibrium if its electrochemical potential is constant throughout the system ($\nabla\tilde{\mu} = 0$). (This presupposes that the defect is sufficiently mobile over the appropriate time and length scales.) For the electroneutral bulk and the space-charge layers, characterized in the model by spatially invariant values of $\mu^{\ominus}$, this means that the equilibrium concentration profiles in the space-charge layers take the form (with $\alpha = e/k_BT$).

$$c_v(x) = c_v^b e^{-2\alpha[\phi(x)-\phi^b]} \tag{2a}$$

$$c_a(x) = c_a^b e^{\alpha[\phi(x)-\phi^b]}. \tag{2b}$$

2.1 | Simple analytical expressions for R^{gb}

A measured conductivity contains contributions from all mobile charge carriers, electronic and ionic. Which contributions need to be taken into account for the CeO_2-M_2O_3 system? In the present case—oxidizing conditions, intermediate (measurement) temperatures—the contributions from electrons to the bulk and grain-boundary conductivities can be ignored. For the bulk phase, the electronic conductivity is orders of magnitude lower than the ionic conductivity (the materials are excellent oxide-ion conductors). In the space-charge layers, electron accumulation may be significant, but there can be no contribution to the measured grain-boundary resistance, since an ionic current cannot be transformed into an electronic current within a material (the ionic and electronic rails run in parallel[86]). In addition, the contributions to measured conductivities from the cations can be safely ignored, since, as noted above, they have negligible mobility at intermediate (measurement) temperatures. Consequently, only oxygen vacancies need to be taken into account when considering the measured conductivities.

The resistance of a single grain boundary, R^{gb}, when considered as an excess quantity, is the total resistance of a system containing a bulk phase, one grain-boundary core and two space-charge layers minus the resistance of a grain of identical dimensions without grain boundary and space-charge layers ($R^{gb} = R^t - R^b = 2R^{scl} + R^c$). Assuming the resistance of the core to be negligible ($2R^{scl} \gg R^c$), we can express R^{gb} as follows:

$$R^{gb} = \frac{2}{A}\left(\int_0^L \frac{1}{\sigma_v(x)}dx - \int_0^L \frac{1}{\sigma_v^b}dx\right), \tag{3}$$

where $\sigma_v(x)$ is the local oxygen-vacancy conductivity and σ_v^b, its value in the bulk. A is the cross-sectional area of the grain. The grain extends from $x = 0$ to $x = 2L$, with identical space-charge layers at $x = 0$ and $x = 2L$. Hence, the grain is symmetrical about $x = L$, and only the portion between $x = 0$ and $x = L$ needs to be considered. The grain half-width L is considered to be large compared with the extent of the space-charge zone, such that bulk defect concentrations are found at $x = L$.

The local oxygen-vacancy conductivity $\sigma_v(x)$ can be expressed as the product of the vacancies' concentration $c_v(x)$, charge $2e$ and mobility u_v, that is,$\sigma_v(x) = c_v(x)2eu_v$. Since, as one of the two main assumptions, u_v is taken to be constant up to the core, the factor $(1/u_v)$ can be moved outside the integrals of Equation 3. In addition, since electrochemical equilibrium is assumed for the vacancies ($\nabla\tilde{\mu}_v = 0$), $c_v(x)$ is related to c_v^b through Equation 2a, and the factor $(1/c_v^b)$ can be moved outside the integrals, too. In this way, Equation 3 becomes,

$$R^{gb} = \frac{2}{A\sigma_v^b}\int_0^L \left(e^{2\alpha[\phi(x)-\phi^b]} - 1\right) dx. \tag{4}$$

The potential distribution, $\phi(x) - \phi^b$, is found by solving the Poisson equation,

$$\varepsilon_0\varepsilon_r \frac{d^2\phi}{dx^2} = ec_a(x) - 2ec_v(x), \tag{5}$$

for the boundary conditions $\Phi_0 = \phi(0) - \phi^b$ and $\nabla\phi^b = 0$. The critical issue, as noted above, is the behavior of the dopant: Gouy-Chapman corresponds to $\nabla\tilde{\mu}_a = 0$; Mott-Schottky corresponds to $\nabla c_a = 0$. In each case the aim when solving Equation 5 is to obtain an expression for $\phi(x) - \phi^b$ that, upon substitution into Equation 4, gives a form amenable to analytical integration.

2.2 | Gouy-Chapman (GC) space-charge layers

For the case of both point defects being mobile, we can substitute Equation 2 into Equation 5 to give,

$$\frac{d^2\phi}{dx^2} = \frac{1}{2\alpha\ell_D^2}\left(e^{\alpha[\phi(x)-\phi^b]} - e^{-2\alpha[\phi(x)-\phi^b]}\right), \tag{6}$$

where ℓ_D is the Debye length,

$$\ell_D = \sqrt{\frac{\varepsilon_0\varepsilon_r k_B T}{2e^2 c_a^b}}. \tag{7}$$

Writing Equation 6 in this way emphasizes that ℓ_D emerges naturally as the characteristic length[87].

Equation 6 does not have an analytical solution. Numerical solutions can be easily obtained for all values of Φ_0, but only those numerical solutions for which $\alpha\Phi_0 < \ln[N_a^b/c_a^b]$ are physically reasonable, that is, for values of Φ_0 such that the dopant concentration at the interface does not exceed the number of cation sites, $c_a^b e^{\alpha\Phi_0} < N_a^b$. With $c_a^b/N_a^b = 1\%$ at $T = 713$ K, for example, physically reasonable values of the space-charge potential are limited to $\Phi_0 < 0.28$ V. One can avoid this problem by replacing the Maxwell-Boltzmann form of Equation 1b {containing $k_B T \ln n_a$} with a Fermi-Dirac-type expression {containing $k_B T \ln[n_a/(1 - n_a)]$}, which takes site exclusion into account. This does not lead, however, to a simple expression for $\phi(x)$, and consequently, for R^{gb}.

An analytical solution is possible by making the depletion approximation: the concentration of the depleted species (oxygen vacancies) is neglected in Equation 6. This is a reasonable approximation, since the contribution of the depleted charge carriers to the charge density is small compared to that from the accumulated acceptor dopants. The resultant Poisson equation has the solution[87]

$$\phi(x) - \phi(L) = \begin{cases} \Phi_0 - \frac{2}{\alpha}\ln\left(1 + \frac{x}{2\ell_D}e^{\alpha\Phi_0/2}\right), & 0 \le x \le 2\ell_D \\ 0, & 2\ell_D < x \end{cases} \tag{8}$$

In order to show how reasonable the depletion approximation is, we compare in Figure 1 the exact (numerical) and approximate (depletion-approximation) solutions to Equation 6. The approximate solution is identical to the exact solution close to the interface, since in this region the depletion approximation is best fulfilled, $c_v(x) \ll c_a(x)$. Further from the

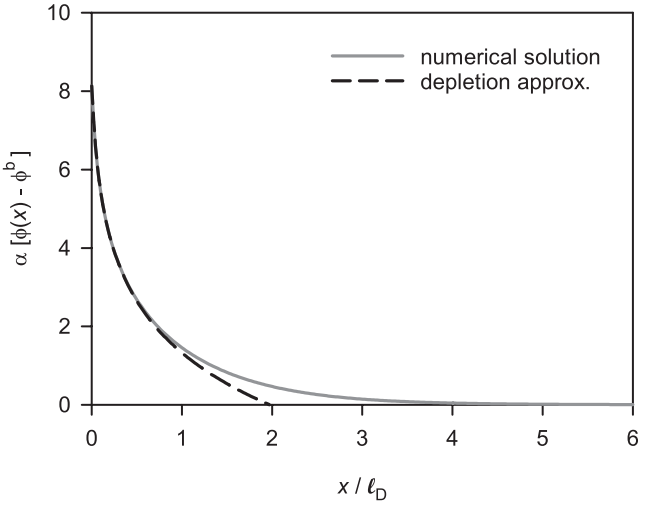

FIGURE 1 Dimensionless space-charge potential plotted against normalised spatial coordinate for a Gouy-Chapman space-charge layer: comparison of numerical (exact) and depletion-approximation solutions to the Poisson equation, Equation 6. ℓ_D is the Debye screening length; $\alpha = e/k_B T$

interface, the approximate solution deviates from the numerical solution, as the concentration of vacancies approaches that of the dopant and the depletion approximation loses validity.

Substitution of Equation 8 into Equation 4 and integrating over $x = 0 \ldots 2\ell_D$ (the region for which Equation 8 is valid) gives,

$$R_{GC}^{gb} = \frac{4\ell_D}{3A\sigma_v^b}\left[e^{3\alpha\Phi_0/2} - \frac{e^{3\alpha\Phi_0/2}}{(e^{\alpha\Phi_0/2}+1)^3} - 3\right]. \quad (9)$$

For values of $\alpha\Phi_0 > 3$, the two latter terms within the square brackets are negligible, and one obtains

$$R_{GC}^{gb} \approx \frac{4\ell_D}{3A\sigma_v^b} e^{3\alpha\Phi_0/2}. \quad (10)$$

The analysis of experimental data is often based on the ratio of the grain-boundary to bulk resistance, R^{gb}/R^b. In the Gouy-Chapman case, this ratio follows from Equation 10 as (note the grain size of $2L$).

$$\left(\frac{R^{gb}}{R^b}\right)_{GC} \approx \frac{2\ell_D}{3L} e^{3\alpha\Phi_0/2}. \quad (11)$$

In Figure 2 we compare the resistance ratio obtained numerically by integration (first, of the Gouy-Chapman Poisson equation, Equation 6, and then, of Equation 4) with the approximate value from Equation 11. We see that Equation 11 is a remarkably good approximation down to $\alpha\Phi_0 \approx 0.8$. A closer examination of the data (not shown) indicates that, for $0.8 \le \alpha\Phi_0 \le 10$, Equation 11 underestimates the resistance ratio by less than 3%. Alternatively, using Equation 11 to analyze resistance ratios yields values of $\alpha\Phi_0$ that are overestimated by up to 6% for $0.8 \le \alpha\Phi_0 \le 3$ but by less than 1% for $3 \le \alpha\Phi_0 \le 10$.

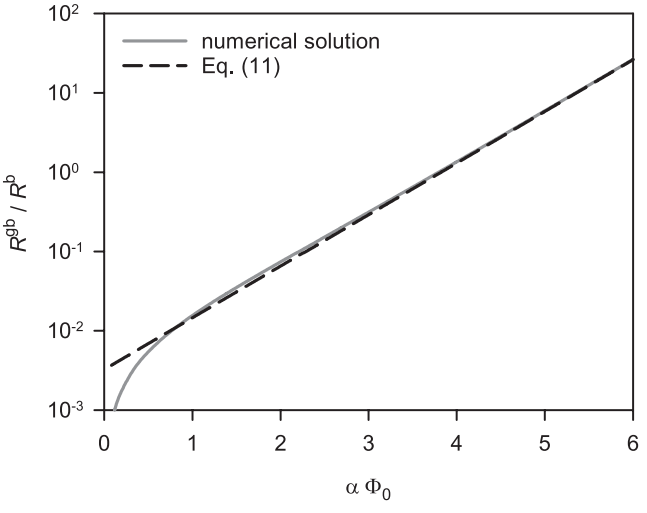

FIGURE 2 The ratio of grain-boundary to bulk resistance, R^{gb}/R^b, for Gouy-Chapman space-charge layers as a function of dimensionless potential, $\alpha\Phi_0$: comparison of numerical (exact) values with the analytical expression of Equation 11. Calculations performed with $\ell_D = 4.88$ nm and $2L = 2$ μm

2.3 | Mott-Schottky (MS) space-charge layers

One widely held misconception is that the alternative extreme case—a Mott–Schottky space-charge layer—refers to the dopant being immobile. This is incorrect. It refers to the dopant's concentration being fixed at its bulk value. Dopant immobility is of course required for the concentration to be constant, but it is not the defining condition.

With $c_a(x) = c_a^b$, Equation 5 becomes,

$$\frac{d^2\phi}{dx^2} = \frac{1}{2\alpha\ell_D^2}\left(1 - e^{-2\alpha[\phi(x)-\phi^b]}\right). \quad (12)$$

Neglecting, as before, the depleted charge carriers (the exponential term) and integrating twice, one obtains,

$$\phi(x) - \phi^b = \begin{cases} \Phi_0\left(\frac{x}{\ell_{MS}} - 1\right)^2, & 0 \le x \le \ell_{MS} \\ 0, & \ell_{MS} < x \end{cases} \quad (13)$$

ℓ_{MS}, the Mott-Schottky screening length, is given by,

$$\ell_{MS} = \sqrt{\frac{2\varepsilon_0\varepsilon_r\Phi_0}{ec_a^b}} = \ell_D\sqrt{4\alpha\Phi_0}. \quad (14)$$

Unfortunately, substitution of Equation 13 into Equation 4 does not yield an expression that can be easily integrated ($\int e^{x^2} dx$). In this case, a further approximation is required: By linearizing the electric potential of Equation 13, to give $\phi(x) - \phi^b = \Phi_0[1 - 2x/\ell_{MS}]$,* the integral of Equation 4 can be evaluated, and one obtains,

$$R_{MS}^{gb} = \frac{2\ell_{MS}}{A\sigma_v^b}\left[\frac{\sinh(2\alpha\Phi_0)}{2\alpha\Phi_0} - 1\right]. \quad (15)$$

For values of $\alpha\Phi_0 > 3$, the first term in the square brackets dominates and the sinh function can be approximated by a single exponential, leading to,

$$R_{MS}^{gb} \approx \frac{2\ell_{MS}}{A\sigma_v^b}\frac{e^{2\alpha\Phi_0}}{4\alpha\Phi_0} = \frac{2\ell_D}{A\sigma_v^b}\frac{e^{2\alpha\Phi_0}}{\sqrt{4\alpha\Phi_0}}. \quad (16)$$

The ratio of grain boundary to bulk resistance, R^{gb}/R^b, in this case follows from Equation 16 as follows:

$$\left(\frac{R^{gb}}{R^b}\right)_{MS} \approx \frac{\ell_D}{L}\frac{e^{2\alpha\Phi_0}}{\sqrt{4\alpha\Phi_0}}. \quad (17)$$

*NB: Potential profiles for the MS depletion approximation and linearized depletion approximation plotted in Figure 8 of Göbel et al[83] are incorrect.

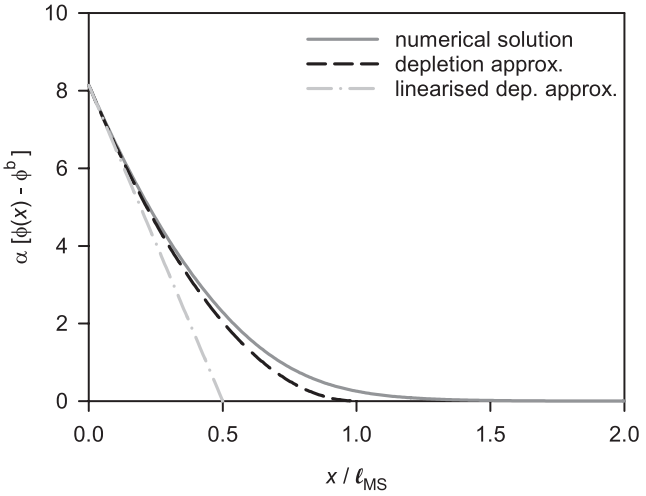

FIGURE 3 Dimensionless space-charge potential plotted against normalised spatial coordinate for a Mott-Schottky space-charge layer: comparison of numerical (exact), depletion-approximation and linearized depletion-approximation solutions to the Poisson equation, Equation 12. ℓ'_{MS} is the Mott-Schottky screening length; $\alpha = e/k_B T$

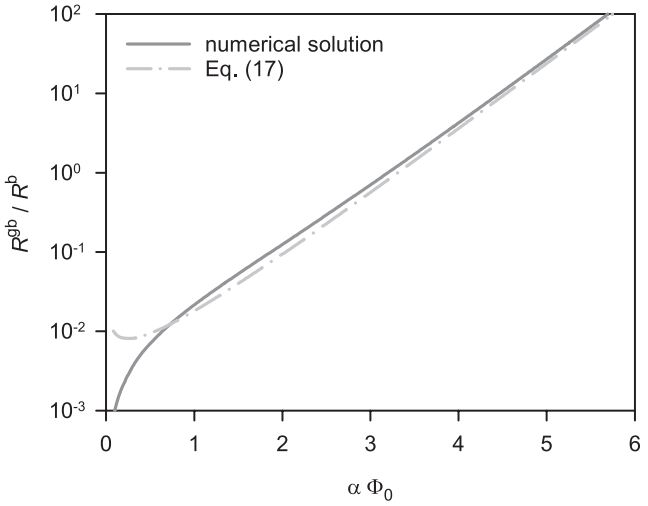

FIGURE 4 The ratio of grain-boundary to bulk resistance, R^{gb}/R^{b}, for Mott-Schottky space-charge layers as a function of dimensionless potential, $\alpha\Phi_0$: comparison of numerical (exact) values with the analytical expression of Equation 17. Calculations performed with $\ell'_D = 4.88$ nm and $2L = 2$ μm

A comparison of the exact (numerical) and two approximate solutions to Equation 12 is given in Figure 3. Again, the depletion approximation yields a relatively good description of $\phi(x)$ close to the interface, with slight deviations at the edge of the space-charge layer, where the depletion approximation does not hold. The linearized depletion approximation provides a poor description of $\phi(x)$, describing only the potential distribution close to the interface. Nevertheless, the analytical expression derived for R^{gb}/R^{b} from the linearised depletion approximation (Equation 17) gives a surprisingly good approximation (see Figure 4) of the resistance ratio obtained numerically by integration (first, of the Mott-Schottky Poisson equation, Equation 12, and then, of Equation 4). This is because the most resistive part of an MS space-charge layer is that part closest to the interface (the local resistivity in a space-charge layer depending exponentially on $\phi(x) - \phi^{b}$, see Equation 4), and this part is described well by the linearized depletion approximation.

Comparing Figures 2 and 4, we see that, in the MS case, the analytical expression gives resistance ratios that underestimate the numerical (exact) values to a much larger degree for $\alpha\Phi_0 > 0.8$. The detailed analysis (not shown) indicates a difference of up to 12% for $0.8 \le \alpha\Phi_0 \le 10$ but below 5% for $10 \le \alpha\Phi_0 \le 30$. Alternatively, for a given value of R^{gb}/R^{gb}, $\alpha\Phi_0$ is overestimated by up to 12% for $0.8 \le \alpha\Phi_0 \le 3$ but by less than 5% for $3 \le \alpha\Phi_0 \le 10$.

2.4 | Interfacial thermodynamics

The quantity reported most often to characterize space-charge layers at grain boundaries in ion-conducting oxides is the space-charge potential Φ_0. It is easily determined by applying, for example, Equation 17 to experimental resistance ratios. Sometimes it is used as a simple test of reasonableness: If values of Φ_0 obtained in an analysis are similar to those reported in the literature for other oxide-ion conducting systems (not necessarily referring to the same materials system, let alone the same composition), then the results are regarded as reasonable. Φ_0, however, is neither specific to a material nor specific to a particular interface. For a given interface, it will vary with the thermodynamic variables (eg, temperature and dopant concentration). For given thermodynamic variables, it will vary with the atomistic structure of the grain boundary, and thus, with the grain-boundary orientation.[88–91] Values of Φ_0 obtained for ceramics are thus weighted averages over the type, frequency and spatial distribution of grain boundaries in the ceramic sample. The quantities that are specific to a material and to interfaces are the differences in the standard chemical potentials of the defects between bulk and core, $\Delta\mu^{\ominus}_{def} = \mu^{\ominus,c}_{def} - \mu^{\ominus,b}_{def}$. These differences constitute the thermodynamic driving energies for space-charge formation.

The space-charge potential can be predicted from a given set of $\Delta\mu^{\ominus}_{def}$ by coupling the interfacial defect thermodynamics to the bulk defect thermodynamics. Essentially, one assumes that the mobile point defects are in electrochemical equilibrium between core and bulk phases, $\tilde{\mu}^{c}_{def} - \tilde{\mu}^{b}_{def} = 0$, subject to the condition that the charge (per unit area) of the grain-boundary core is compensated by the two space-charge layers, $Q^{c} + 2Q^{scl} = 0$. Generally, for a system containing two charge carriers, these two contributions can be written[7] as (w^{c} is the core's width),

$$Q^{c} = w^{c}\left[2e(c^{c}_{v} - c^{b}_{v}) - e(c^{c}_{a} - c^{b}_{a})\right]$$
$$Q^{scl} = \int_{0}^{L}\left[2ec_{v}(x) - ec_{a}(x)\right]\mathrm{d}x \qquad (18)$$

Let us first briefly sketch out the procedure of calculating Φ_0 from given $\Delta\mu_{\rm def}^{\ominus}$, taking as our example the case of Mott-Schottky space-charge layers. With the help of Equation 1a, one can re-write Equation 18 as follows:

$$\begin{aligned} Q_{\rm MS}^{\rm c} &= w^{\rm c} e c_{\rm a}^{\rm b}\left[\left(\frac{N_{\rm v}^{\rm c}}{N_{\rm v}^{\rm b}}\right)\mathrm{e}^{-\alpha(2\Phi_0+\Delta\mu_{\rm v}^{\ominus}/e)}-1\right] \\ Q_{\rm MS}^{\rm scl} &= e c_{\rm a}^{\rm b}\int_0^L\left[\mathrm{e}^{-2\alpha[\phi(x)-\phi^{\rm b}]}-1\right]\mathrm{d}x. \end{aligned} \tag{19}$$

To evaluate the integral, one requires the electric potential profile, $\phi(x)-\phi^{\rm b}$, and this can only be obtained exactly by solving numerically Equation 12 (the relevant Poisson equation). Obtaining a self-consistent solution requires, therefore, an iterative procedure,[6,7] in which Φ_0 is varied (with Equation 12 being solved and Equation 19 being evaluated) until $Q_{\rm MS}^{\rm c}+2Q_{\rm MS}^{\rm scl}=0$ is fulfilled to required accuracy.

This procedure is not undemanding because $\phi(x)-\phi^{\rm b}$ has to be calculated numerically in every single iteration cycle. A preferable procedure would avoid this, and here we present a closed-form solution. A single integration of Equation 12 and subsequent application of Gauss' Law yields namely[92,93]

$$Q_{\rm MS}^{\rm scl} = -2ec_{\rm a}\ell_{\rm D}\sqrt{\left(\alpha\Phi_0-\frac{1}{2}\right)}. \tag{20}$$

Thus, combining $Q_{\rm MS}^{\rm c}$ from Equation 19 and $Q_{\rm MS}^{\rm scl}$ from Equation 20 according to $Q_{\rm MS}^{\rm c}+2Q_{\rm MS}^{\rm scl}=0$ results in a single equation with one unknown (Φ_0) that can be solved for given T, $c_{\rm a}^{\rm b}$, $N_{\rm v}^{\rm b}$, $N_{\rm v}^{\rm c}$, $w^{\rm c}$, and $\Delta\mu_{\rm v}^{\ominus}$. Although this simple short-cut avoids determining the exact form of $\phi(x)-\phi^{\rm b}$, it is nevertheless mathematically exact.

In the case of Gouy-Chapman space-charge layers, the relevant equations are as follows:

$$\begin{aligned} Q_{\rm GC}^{\rm c} &= w^{\rm c} e c_{\rm a}^{\rm b}\left[\left(\frac{N_{\rm v}^{\rm c}}{N_{\rm v}^{\rm b}}\right)\mathrm{e}^{-\alpha(2\Phi_0+\Delta\mu_{\rm v}^{\ominus}/e)}\right. \\ &\quad\left.-\left(\frac{N_{\rm a}^{\rm c}}{N_{\rm a}^{\rm b}}\right)\mathrm{e}^{\alpha(\Phi_0+\Delta\mu_{\rm a}^{\ominus}/e)}\right] \\ Q_{\rm GC}^{\rm scl} &= -4ec_{\rm a}^{\rm b}\ell_{\rm D}\sinh\left(\frac{\alpha\Phi_0}{2}\right) \end{aligned} \tag{21}$$

The considerations in this section have employed the Maxwell-Boltzmann forms of Equation 1 in Equations 19 and 21 for consistency, but we recommend using Fermi-Dirac expressions for the electrochemical potentials of the defect building units, in order to avoid physically unreasonable defect concentrations.

Lastly, we note that Maier and co-workers include a gap between core and bulk phases.[3,8,87] Their arguments for the inclusion of a gap are essentially phenomenological, that is, that certain grain-boundary properties can only be described with a thermodynamic model when a gap is included. In contrast, examination of grain-boundary structures obtained experimentally from TEM or obtained by atomistic modelling reveal no such gap. It appears, therefore, that the inclusion of such a gap serves only to account for non-ideal thermodynamic behavior.

3 | POISSON-CAHN THEORY

For a system of point defects that exhibits deviations from dilute-solution behavior, one traditionally accounts for the deviations by introducing defect associates into the thermodynamic description of the system. Thus for the present case, in addition to considering acceptor dopants (a) and oxygen vacancies (v) as defect chemical species, one introduces dopant-vacancy associates, such as a-v pairs and a-v-a trios. By specifying equilibrium constants for the respective defect association reaction(s), one can, in principle, achieve a quantitative description of the point-defect thermodynamics. One may, however, obtain enthalpies of defect association that vary with acceptor concentration, and one may have to introduce even higher order associates arbitrarily with increasing acceptor concentration.

There is also a conceptual problem in seeking to extend the standard dilute-solution approach by introducing defect associates. The idea of acceptor species trapping vacancies makes no sense at high acceptor concentrations because the vacancies can never be free: they are always trapped. Moving away from one acceptor cation in a solid solution, a vacancy finds itself immediately next to another acceptor cation. For a trapping model to be applicable, vacancies need to be able to reside at lattice positions away from the influence of the acceptor cations.

The need to move beyond dilute-solution treatments for interfaces is impelled, therefore, in part by dilute-solution treatments of the bulk phase being inadequate or unsatisfactory. Indeed, current models of the bulk properties of CeO_2-Gd_2O_3 materials require far more complex approaches than simply introducing defect associates.[94–97] The need to move beyond dilute-solution treatments is also impelled in part by the very presence of an interface in a system of interacting species[98,99] (see Section 3.1). And it is impelled by two substantial deficiencies in the dilute-solution descriptions of interfacial behavior. One deficiency concerns the extent of acceptor-cation accumulation at grain boundaries in ceria solid solutions. Experimentally they are found to extend several nanometers;[38,60,64,65] the Debye length (Equation 7) of the dilute-solution approach predicts, in contrast, values of only a few angstroms. This deficiency cannot be remedied by including a-v pairs and a-v-a trios. The second deficiency concerns the spatial variation of oxygen vacancies in space-charge layers. APT studies[66] of grain boundaries in

$Ce_{0.9}Nd_{0.1}O_{1.95}$ and $Ce_{0.7}Nd_{0.3}O_{1.85}$, as well as atomistic simulations of grain boundaries[53] and surfaces[100,101] in Gd_2O_3-substituted CeO_2, find co-accumulation of acceptor cations and oxygen vacancies. It is impossible for such behavior—co-accumulation of oppositely charged defects—to emerge from a dilute-solution approach (see Equation 1). There is little doubt, therefore, that a new approach is necessary.

Our approach to this problem, essentially, is to restrict the thermodynamic description to the two fundamental defect species, a and v, (in order to keep the same basic formulism) but to replace the site fractions of the dilute approximation with chemical activities. Poisson-Cahn theory constitutes one method for calculating activity coefficients for a and v as a function of temperature and composition. And it does so consistently across the entire compositional range. For dilute solutions, the activity coefficients reduce to unity, and for the case of mobile a and v, Gouy-Chapman behavior (see Section 2.2) is obtained, as it should (this being one benefit of keeping the same basic formalism); for concentrated solid solutions, in contrast, the activity coefficients deviate substantially from unity, and complex behavior may emerge.[76,80]. In the following section, we present Poisson-Cahn theory in detail.

3.1 | Variational formulation

We focus on the same system as in Section 2, that is, with two charge carriers (a and v). Poisson-Cahn theory, it is stressed, is not restricted to only two charge carriers, and we have already extended the theory elsewhere[80] to include electronic charge carriers. Here, the restriction to two charge carriers is made so that the Poisson-Cahn results can easily be compared with those from the standard dilute-solution approaches. We also focus, as in Section 2, on a grain extending from $x = 0$ to $x = 2L$ with two identical space-charge layers. Here, the core has to be included explicitly from the beginning, but to keep the two cases comparable and for the sake of simplicity, we assume that the core has no width. This assumption can be discarded if the need arises, but it does serve to keep the following derivation relatively simple.

We begin by considering the total free energy of the non-homogeneous system between $x = 0$ and $x = 2L$. Again, since the grain is symmetrical about $x = L$, only the portion between $x = 0$ and $x = L$ needs to be considered. The inhomogeneity of the system makes this free energy a functional:

$$\begin{aligned}\mathcal{F}[n_{\mathrm{v}},n_{\mathrm{a}},\phi;T,n_{\mathrm{a}}^{\mathrm{b}}] &= \Gamma_{\mathrm{v}}^{\mathrm{c}}\Delta\mu_{\mathrm{v}}^{\ominus}n_{\mathrm{v}}(0)+\Gamma_{\mathrm{a}}^{\mathrm{c}}\Delta\mu_{\mathrm{a}}^{\ominus}n_{\mathrm{a}}(0)\\ &+\int_0^L\Big\{g(n_{\mathrm{a}},n_{\mathrm{v}},T)+e\phi(2N_{\mathrm{v}}^{\mathrm{b}}n_{\mathrm{v}}-N_{\mathrm{a}}^{\mathrm{b}}n_{\mathrm{a}})\\ &-N_{\mathrm{a}}^{\mathrm{c}}k_{\mathrm{B}}T\left[n_{\mathrm{a}}\ln n_{\mathrm{a}}+(1-n_{\mathrm{a}})\ln(1-n_{\mathrm{a}})\right.\\ &\qquad\left.+2n_{\mathrm{v}}\ln n_{\mathrm{v}}+2(1-n_{\mathrm{v}})\ln(1-n_{\mathrm{v}})\right]\\ &+\frac{1}{2}B_{\mathrm{a}}\left(\frac{\mathrm{d}n_{\mathrm{a}}}{\mathrm{d}x}\right)^2+\frac{1}{2}B_{\mathrm{v}}\left(\frac{\mathrm{d}n_{\mathrm{v}}}{\mathrm{d}x}\right)^2-\frac{1}{2}\varepsilon_{\mathrm{r}}\varepsilon_0\left(\frac{\mathrm{d}\phi}{\mathrm{d}x}\right)^2\Big\}\,\mathrm{d}x\end{aligned} \tag{22}$$

where Γ^{c} are the areal densities of sites characterized by $\Delta\mu_{\mathrm{def}}^{\ominus}$ within the core; the function g is the excess free energy due to defect interactions; and the coefficients B are gradient energy coefficients. Here, we assume that g takes the form,

$$g = N_{\mathrm{vv}}\frac{1}{2}f_{\mathrm{vv}}n_{\mathrm{v}}^2+N_{\mathrm{aa}}\frac{1}{2}f_{\mathrm{aa}}n_{\mathrm{a}}^2+N_{\mathrm{aa}}f_{\mathrm{av}}n_{\mathrm{v}}n_{\mathrm{a}}, \tag{23}$$

where f_{ij} is an association free energy between the species i and j, and N_{ij} is the bond density.

It is worth devoting a few words to the gradient energy terms of Equation 22. The concept of a gradient energy in a solid solution was introduced by Cahn in the context of a miscibility gap in a phase diagram that leads to spinodal decomposition.[77] Such a miscibility gap is one source of symmetry breaking—in this context meaning a departure of the average solute lattice configuration from the space-group symmetry of the host lattice—but others may arise from external fields such as those imposed on the system by the presence of extended defects. In such situations there must be a positive gradient energy contribution to the free energy, for the simple reason that the homogeneous solution is not otherwise stable. One can imagine a microscopic explanation for this phenomenon in terms of the ensemble of solute configurations that characterizes the free energy minimum in the homogeneous state. These configurations will extend infinitely in space, and hence, an external field inducing an inhomogeneous solute concentration will necessarily cause the system's free energy to increase. That long-range configurations result from short-range forces is well understood in statistical mechanics: the same principles explain why the long-range effects of gradient energies have their origin in short-range solute interactions.[102] In summary, the inclusion of gradient energy terms for an inhomogeneous concentrated solid solution is a thermodynamic necessity.

Recently, Vikrant et al[103] predicted defect concentrations in ceria solid solutions neglecting gradient energy terms but introducing elastic energy terms into their free energy functional.[†] Such terms arise, essentially, from point defects possessing non-zero formation volumes.[104] In our study, we neglect elastic effects for simplicity, so that we can focus on our main theme, the analysis of the grain-boundary resistance in a thermodynamically consistent manner.

Let us now return to the free energy functional, Equation 22. The equilibrium state of the system is given by the functions n_{v}, n_{a}, and ϕ that minimize the functional, subject to the mass-conservation constraints.

[†] Vikrant et al[103] claim surprisingly that gradient energy coefficients are "experimentally unmeasurable." This is incorrect: they are measurable in the same way that thermodynamic driving energies of space-charge formation, interaction energies between point defects and diffusion coefficients are measurable. That is, by fitting a mathematical model to experimental data in order to extract the required parameter.

$$\int_0^L \left[n_v(x) - n_v^b\right] dx = 0 \tag{24}$$

$$\int_0^L \left[n_a(x) - n_a^b\right] dx = 0 \tag{25}$$

Standard variational calculus yields the Euler-Lagrange equations for the minimizing functions:

$$\frac{1}{N_a^b}\frac{\partial g}{\partial n_a} + k_B T \ln \frac{n_a}{1-n_a} - e\phi - \beta_a \frac{d^2 n_a}{dx^2} = \lambda_a \tag{26}$$

$$\frac{1}{N_v^b}\frac{\partial g}{\partial n_v} + k_B T \ln \frac{n_v}{1-n_v} + 2e\phi - \beta_v \frac{d^2 n_v}{dx^2} = \lambda_v \tag{27}$$

$$\varepsilon_r \varepsilon_0 \frac{d^2\phi}{dx^2} = e(2N_v^b n_v - N_a^b n_a) \tag{28}$$

where $\beta_x = B_x / N_x^b$. We term these equations the Poisson-Cahn equations. The expressions on the left-hand side of Equations 26 and 27 are the electrochemical potentials for inhomogeneous systems, meaning that the constants on the right—the Lagrange multipliers—are the electrochemical potentials in the bulk. These three equations are subject to the boundary conditions.

$$B_a \frac{dn_a}{dx}\Big|_{x=0} = \Gamma_a^c \Delta\mu_a^{\ominus} \tag{29}$$

$$\frac{dn_a}{dx}\Big|_{x=L} = 0 \tag{30}$$

$$B_v \frac{dn_v}{dx}\Big|_{x=0} = \Gamma_v^c \Delta\mu_v^{\ominus} \tag{31}$$

$$\frac{dn_v}{dx}\Big|_{x=L} = 0 \tag{32}$$

$$\frac{d\phi}{dx}\Big|_{x=0} = \frac{d\phi}{dx}\Big|_{x=L} = 0 \tag{33}$$

The boundary conditions in the oxide bulk are the bulk defect concentrations and the reference electrostatic potential. Because the theory does not consider the grain-boundary core to exist as a separate phase, there is no charge separation outside of the interval [0, L], and the derivative of the electrostatic potential is therefore zero at the interface.

The model so formulated is a second-order, nonlinear boundary value problem (retaining the elliptic character of the Poisson-Boltzmann model) that can be solved with standard techniques. The results presented in the subsequent section were generated with a custom-built, adaptive finite-elements solution implemented in MATLAB.

Parameters used in the simulations appear in Table 1. They probably do not constitute a unique set: another set may give an equally good, if not better, description of the system. Some parameters appearing in Table 1 have been drawn from first principles calculations—it should be possible to derive first principles estimates for the other parameters as well, including the gradient energy coefficients—however, the theory as utilized in this work is phenomenological. Some of the parameters are substantially different to those published in our previous paper;[76] this is a consequence of considering the restricted equilibrium case for acceptor cations here, but the less realistic case of electrochemical equilibrium for acceptor cations in the previous study.[76] In addition, we are aware that a continuum approach is an approximation that becomes poorer as the space-charge layer and structural extent of the grain boundary become comparable in length. However, continuum theories operating at similar length scales (in particular the Cahn-Hilliard theory itself) have proven successful in the past, and there is currently no straightforward possibility of recourse to an atomistic theory if equilibrium with a bulk phase is desired.

3.2 | Length scale

Experiments indicate that the characteristic length for acceptor accumulation derived from Poisson-Boltzmann theory—the Debye length—does not pertain to concentrated systems in which accumulation layers have been found to be an order of magnitude larger.[38,60,64,65] Since Poisson-Cahn theory yields space-charge layers that extend nanometres,[76,80] rather than angstroms, it is interesting to consider whether a characteristic length may be derived from the theory.

TABLE 1 Parameters used in the Poisson-Cahn simulations

Parameter	Value	Comment
ε_r	35	Relative dielectric permittivity
a_{uc}/Å	5.43	Lattice constant
f_{vv}/eV	0.47	v-v interaction energy*
f_{aa}/eV	1.67	a-a interaction energy*
f_{av}/eV	−1.33	a-v interaction energy*
$\Delta\mu_v^{\ominus}$/eV	−2.20	Drives space-charge formation*
$\Delta\mu_a^{\ominus}$/eV	0	
Γ_v^c/mol m^{-2}	2.38×10^{-5}	Areal density of sites with $\Delta\mu_v^{\ominus}$
N_{vv}/m^{-3}	$3N_v$	
N_{av}/m^{-3}	$8N_a$	
N_{aa}/m^{-3}	$4N_a$	
B_v/eV nm^{-1}	4.56×10^{-5}	Gradient energy coefficient for v*
B_a/eV nm^{-1}	5.06×10^{-4}	Gradient energy coefficient for a*

The symbol (*) indicates that this parameter was varied to reproduce experimental conductivity data.

The Debye length, we recall, emerges naturally as a characteristic length in Poisson-Boltzmann theory (see Equations 6 and 12). In Poisson-Cahn theory, there is no such natural emergence of a characteristic length because we have a systems of linked Equations 26–28, each of which shows some mathematically complexity. We may also recall[105,106] that the Debye length can be obtained by linearizing a Poisson-Boltzmann expression (for a dilute solution of two mobile, equally charged species). We follow, therefore, an analogous route to obtain a characteristic Poisson-Cahn length. We linearise the system of Equations 26–28 about the bulk values n_a^b and n_v^b, using the local excess free energy of Equation 23 and extending the domain to $L=\infty$. We thus obtain the linear system.

$$\beta_a \frac{d^2 n_a}{dx^2} = \left[\frac{k_B T}{n_a^b(1-n_a^b)} + \nu_{aa} f_{aa}\right] \times (n_a - n_a^b) + \nu_{av} f_{av}(n_v - n_v^b) - e\phi \tag{34}$$

$$\beta_v \frac{d^2 n_v}{dx^2} = \nu_{va} f_{av}(n_a - n_a^b) + \left[\frac{k_B T}{n_v^b(1-n_v^b)} + \nu_{vv} f_{vv}\right] \times (n_v - n_v^b) + 2e\phi \tag{35}$$

$$\varepsilon_r \varepsilon_0 \frac{d^2\phi}{dx^2} = e[N_a^b(n_a - n_a^b) - 2N_v^b(n_v - n_v^b)] \tag{36}$$

with the solution,

$$\begin{bmatrix} (n_a - n_a^b) \\ (n_v - n_v^b) \\ \phi \end{bmatrix} = \sum_{i=1}^{3} k_i \xi_i \exp\left(-\frac{x}{\ell_i}\right) \tag{37}$$

where k_i are constants determined by boundary conditions and ξ_i and $1/\ell_i^2$ are the eigenvectors and eigenvalues, respectively, of the matrix.

$$\begin{bmatrix} \beta_a & 0 & 0 \\ 0 & \beta_v & 0 \\ 0 & 0 & \varepsilon_r\varepsilon_0 \end{bmatrix}^{-1} \times \begin{bmatrix} \left[\frac{k_B T}{n_a^b(1-n_a^b)} + \nu_{aa} f_{aa}\right] & \nu_{av} f_{av} & -e \\ \nu_{va} f_{av} & \left[\frac{k_B T}{n_v^b(1-n_v^b)} + \nu_{vv} f_{vv}\right] & 2e \\ eN_a^b & -2eN_v^b & 0 \end{bmatrix} \tag{38}$$

with $\nu_{xx} = N_{xx}/N_x^b$, $\nu_{av} = N_{av}/N_a^b$, and $\nu_{va} = N_{av}/N_v^b$.

Equation 37 thus indicates that there are several lengths in Poisson-Cahn theory (one or more of which may be complex, indicative of an oscillatory solution). The maximum length ℓ_{PC}^{max} derived from the eigenvalues of the matrix (38) will dominate the solution of Equation 37 and thus we take it to be the characteristic Poisson-Cahn length. A note of caution is warranted here. Since it has been obtained through linearization, ℓ_{PC}^{max} is only valid in the limit of small effects, that is, it gives the screening length in a homogeneous, concentrated solid solution probed by an infinitesimal charge. Much larger effects, for example, acceptor accumulation in space-charge layers, may not necessarily be characterized by ℓ_{PC}^{max}.

3.3 | Vacancy mobility

One of the two main assumptions of the Poisson-Boltzmann models, as already mentioned in Section 2, is that the mobility of the charge carriers is constant throughout the bulk phase and the space-charge layers. This is a reasonable zero-order assumption for a dilute solution. In the Mott-Schottky case, a and v constitute a dilute solution in the bulk phase, and the concentration of v gets even more diluted in the space-charge zones. The Gouy-Chapman case is more complex because of acceptor accumulation in the space-charge zones. As long as the accumulation profile is accurately described by $c_a^b e^{\alpha[\phi(x)-\phi^b]}$ (cf. Equation 1b), however, the system behaves as a dilute solution. One may say, therefore, that the assumption of a constant mobility is reasonable as long as the composition of the matrix does not change significantly.

In a concentrated solid solution, on the other hand, the composition of the matrix—on both anion and cation sublattices—can change significantly in a space-charge layer. The assumption of constant charge-carrier mobility loses, therefore, its validity. In order to calculate the vacancy mobility as a function of composition (and thus of position within the space-charge layers), we employed the model of Nakayama and Martin.[107] This model considers the association between oxygen vacancies and ionized acceptors, beginning with a defect equilibrium model composed of cation tetrahedra and the accompanying tetrahedrally coordinated anion sites in the fluorite lattice. The acceptor-vacancy interaction energy in the Poisson-Cahn model is thus employed to determine a distribution of tetrahedral configurations found in the lattice. An average activation energy for vacancy hopping between two adjoining tetrahedra is determined through a weighted harmonic mean of Boltzmann factors calculated with the activation enthalpy appropriate to the composition of the cation-cation edge (whether Ce-Ce, Ce-Gd, or Gd-Gd) through which the vacancy must move. The three activation enthalpies and a common attempt frequency were used as fitting parameters. The values are listed in Table 2.

4 | RESULTS

4.1 | Space-charge extent

We begin by considering the evolution of acceptor accumulation profiles at grain boundaries in the CeO_2-Gd_2O_3

TABLE 2 Parameters used in the Nakayama-Martin model[107] to calculate the composition-dependent ionic conductivity of the CeO_2-Gd_2O_3 system

Parameter	Value
ν_0/s^{-1}	1.062×10^{13}
$\Delta H_{mig,v}^{Ce\text{ - }Ce}/eV$	0.682
$\Delta H_{mig,v}^{Ce\text{ - }Gd}/eV$	1.192
$\Delta H_{mig,v}^{Gd\text{ - }Gd}/eV$	1.323

system as a function of acceptor site fraction. With our focus being on the profiles' extent, we compare in Figure 5 profiles predicted from Poisson-Cahn theory for the parameter values appearing in Table 1 with profiles calculated from the Gouy-Chapman model (Equation 6) with the same $n_a(0)/n_a^b$. The two types of profile agree very well at low n_a^b, indicating clearly that Poisson-Cahn theory reduces to Gouy-Chapman theory in the limit of dilute solutions. From $n_a^b \approx 10^{-2}$ onwards, however, the profiles predicted from Poisson-Cahn theory are almost constant in extent, at around 4 nm, whereas the corresponding Gouy-Chapman profiles are far shorter and decrease in a strong and constant manner (Figure 5D-F). In other words, differences in the lengths of the accumulation layers start to appear at $n_a^b \approx 10^{-2}$, and these differences become more prominent with increasing n_a^b.

Keeping these results in mind, let us now consider the characteristic screening lengths. The benefit of calculating a screening length from Poisson-Cahn theory is that it obviates the need to solve the nonlinear Poisson-Cahn equations. Instead, a comparatively simple mathematical procedure is performed—the eigendecomposition of a matrix—and as described in Section 3.2, it is only a 3×3 matrix that needs to be eigendecomposed for a solid solution of two species (a and v). The characteristic Poisson-Cahn length, ℓ_{PC}^{max}, was obtained from the eigenvalues of matrix (38) for the parameter values appearing in Table 1. The data are plotted for two different temperatures in Figure 6A, B, taking the real part of any complex-valued data, and including the Debye length ℓ_D for comparison.

At low n_a^b there is, as required, no difference between ℓ_{PC}^{max} and ℓ_D at either temperature: Poisson-Cahn theory reduces to Gouy-Chapman theory in the dilute limit. As n_a^b increases, one sees from some critical level onwards increasing deviations between the two characteristic lengths. ℓ_D continues to fall, decreasing even below the lattice constant of CeO_2, whereas ℓ_{PC}^{max}, after a short plateau, rises strongly. This behavior is qualitatively, but not quantitatively, similar to that shown in Figure 5. This, then, is the (expected) disadvantage of the linearization required to obtain ℓ_{PC}^{max} (see Section 3.2). We attribute the rise in ℓ_{PC}^{max} with increasing n_a^b to the gradient energy becoming increasingly important. The crossover point—the point at which the Debye length (and thus the dilute-solution approximation) is no longer valid for this system—is at $n_a^b \approx 0.5\%$ at $T = 713$ K and at $n_a^b \approx 1\%$ at $T = 1573$ K (again, similar to the behavior of Figure 5). The data of Figure 6 thus provide a means for determining quantitatively the limit of dilute-solution behavior. Furthermore, it indicates that the critical concentration depends on temperature and that materials with less than 1% bulk acceptor concentration may display the behavior of concentrated systems.

Lastly, we comment on why the Mott-Schottky model (rather than the Gouy-Chapman model) is widely applied in the literature to concentrated solid solutions. Sometimes it is because the Mott-Schottky case is misunderstood as the case of immobile acceptors rather than the case of constant acceptor concentration. Sometimes it is because of the characteristic screening length. Equation 14 indicates that ℓ_{MS} can be much larger than ℓ_D. For example, at $T = 713$ K, and with a modest space-charge potential of only $\Phi_0 = 0.25$ V, one finds $\ell_{MS} \approx 4\ell_D$. The Mott-Schottky approach thus permits the electrical width of a grain boundary to take values that are much larger than the Debye length, and hence, comparable with experiment. That is, ℓ_{MS} can be physically reasonable, while ℓ_D drops below the lattice spacing.

4.2 | Conductivity

In Figure 7A, B we compare literature data[5,17,21,31,50,108] for the total and the bulk conductivity of CeO_2-Gd_2O_3 ceramics at $T = 713$ K. In those cases where no experimental data are available at this temperature, we interpolated or extrapolated as necessary. Some studies only reported the total conductivity, which is why there are more datasets in (A) than in (B). The total conductivity, it is noted, is an effective quantity over bulk and grain boundaries. It can expressed in terms of the resistance ratio as follows:

$$\frac{\sigma^b}{\sigma^t} = \frac{R^{gb}}{R^b} + 1. \tag{39}$$

It is emphasized that the range of acceptor site fractions that we consider in this figure corresponds, in the light of Figure 6, to those outside the dilute regime, that is, $n_a^b \geq 1\%$.

Let us start by examining the data for σ^b in Figure 7B. Small variations between the individual studies are evident, with the variation between minimum and maximum values being less than a factor of 1.4; the maximum conductivity at this temperature is achieved for $n_a^b \approx 0.1$. Turning now to the data for σ^t in Figure 7A, we find more pronounced scatter, with the variation between minimum and maximum values varying by up to a factor of 4; the broad maximum in the total conductivity appears at this temperature at $n_a^b \approx 0.2$.

That the data for σ^t exhibit more pronounced scatter than the σ^b data is to be expected. The former includes

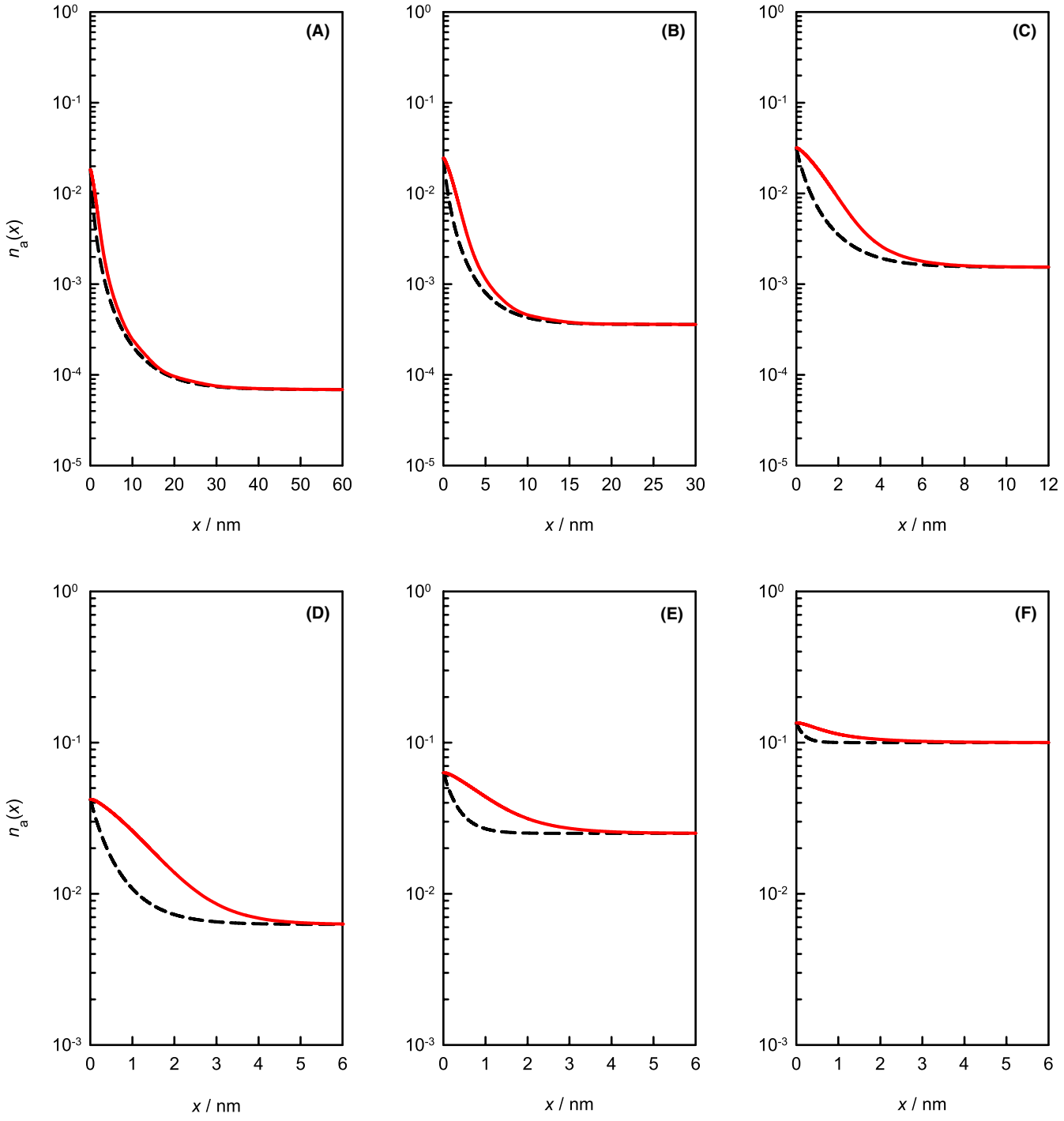

FIGURE 5 Acceptor accumulation profiles in space-charge layers at grain boundaries in the CeO_2-Gd_2O_3 system at $T = 1573$ K. Solid lines refer to the results of Poisson-Cahn simulations. Dashed lines refer to the results of the Gouy-Chapman model

contributions from the grain boundaries, see Equation 39. Samples from various studies will thus be characterized, possibly, by differing grain sizes; by differing amounts and distributions of intergranular porosity; by differing amounts and types of impurities at the grain boundaries; and in particular, by differing degrees of acceptor accumulation resulting from differing thermal histories.

In Figure 7C we plot the ratio σ^b/σ^t (see Equation 39), together with values of the ratio calculated by combining Poisson-Cahn theory and the Nakayama-Martin model for the conductivity (with the set of parameters listed in Tables 1 and 2). Here, we have focussed on describing the data from Tschöpe *et al.*[5] because we know the samples' thermal histories and they are simple: All samples were quenched from $T = 1573$ K. Cooling samples in a furnace from the sintering

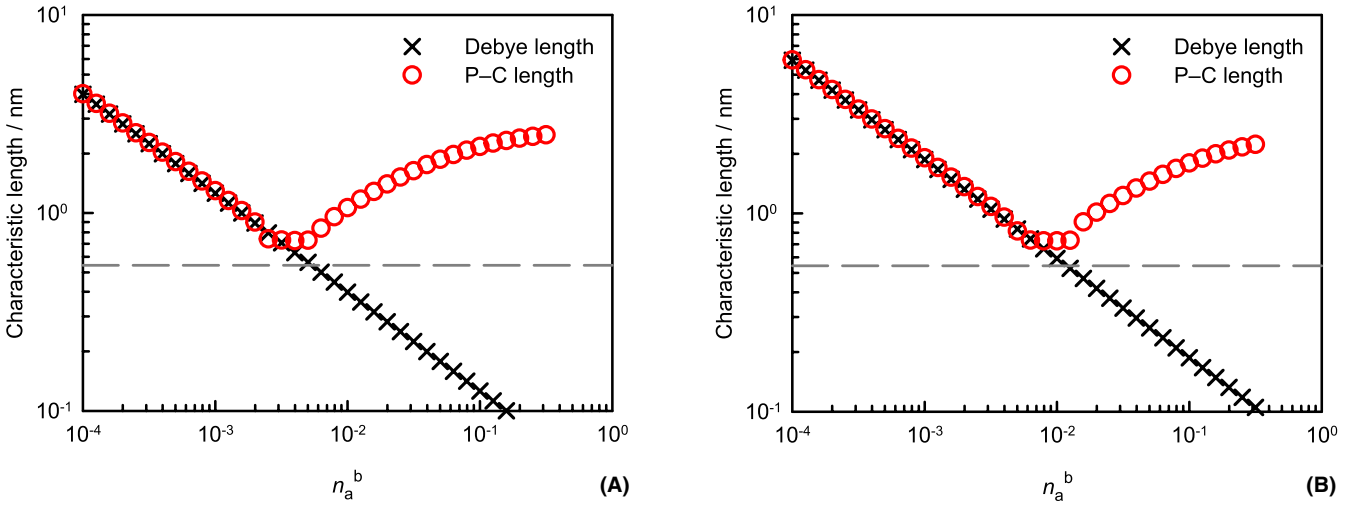

FIGURE 6 Characteristic length scale of space-charge layers in the CeO_2-Gd_2O_3 system obtained from Poisson-Cahn theory (ℓ_{PC}^{max}) against bulk acceptor site fraction n_a^b. Plotted for comparison is the Debye length (ℓ_D). A, $T = 713$ K and (B) $T = 1573$ K. The dashed, horizontal, gray line denotes the lattice parameter of CeO_2

temperature constitutes a far more complicated case, since it is unclear at what the temperature(s) the acceptor accumulation profiles are frozen in.

4.3 | Space-charge potential

The parameter used most often in the literature to characterize space-charge layers is the space-charge potential (see also Section 2.4). Previously, this meant applying dilute-solution theories, even though invalid, to concentrated solutions. Poisson-Cahn theory avoids this inconsistency but generates a different problem: it does not provide a comparatively simple mathematical procedure for extracting the space-charge potential from experimental data, and there is a reason for this.

In Sections 2.2 and 2.3, we saw that the simple functional form of the electrochemical potential of a defect in a dilute solution (Equation 1) allows simple equations relating the grain-boundary resistance to the space-charge potential to be derived. In a concentrated solid solution, a far more complex form is required for the electrochemical potential of a defect, in order to capture the increased complexity of the system. Within Poisson-Cahn theory, the defect electrochemical potential (Equations 26 and 27) contains additional terms that arise from the excess free energy due to defect-defect interactions and from the gradient energy terms. It is, therefore, the necessarily complex functional form of a defect electrochemical potential in a concentrated solid solution that prevents simple procedures from being developed.

Given the lack of alternatives, we examine, consequently, how well the expressions from the dilute-solution theories perform when applied to data obtained for concentrated solutions (ie, outside their region of validity). To this end, we take the conductivity ratios calculated by combining Poisson-Cahn theory and the Nakayama-Martin model (Figure 7C) and extend them down to the dilute-solution regime. We then apply Equations 11 and 17 to obtain Φ_0^{GC} and Φ_0^{MS}, respectively. These data can be compared with values from the Poisson-Cahn simulations, Φ_0^{PC}.

Before we compare the data, let us first consider possible sources of discrepancy between Φ_0^{PC} and Φ_0^{GC} or Φ_0^{MS}. We expect, of course, discrepancies as we cross the boundary between dilute and concentrated solutions; but we also expect discrepancies for the entire range of acceptor concentrations from three separate sources. First, the Poisson-Cahn model that we implemented in this study refers to a restricted equilibrium for the acceptors—equilibrated at $T = 1573$ K but frozen-in at $T = 713$ K—whereas the Poisson-Boltzmann models assume that the acceptors are either in electrochemical equilibrium at $T = 713$ K (Gouy-Chapman) or have a constant concentration (Mott-Schottky). The electrostatic potential profiles in the space-charge zones will thus differ substantially between the two cases. Second, the Nakayama-Martin model necessarily predicts a spatially varying conductivity within the space-charge zones on account of compositional changes; the Poisson-Boltzmann models, in contrast, employ a constant charge-carrier mobility equal to the value in the bulk phase. The values of Φ_0^{GC} and Φ_0^{MS} obtained will thus include the effect of the spatially varying ion mobility. Third, various approximations are made in deriving Equations 11 and 17, and as discussed in Sections 2.2 and 2.3, they also introduce errors.

Bearing these points in mind, we now compare Φ_0^{PC} with Φ_0^{GC} and Φ_0^{MS} as a function of n_a^b in Figure 8. We consider three general regions, without wanting to define strict boundaries between these regions. At low n_a^b, Φ_0^{PC} is close to the

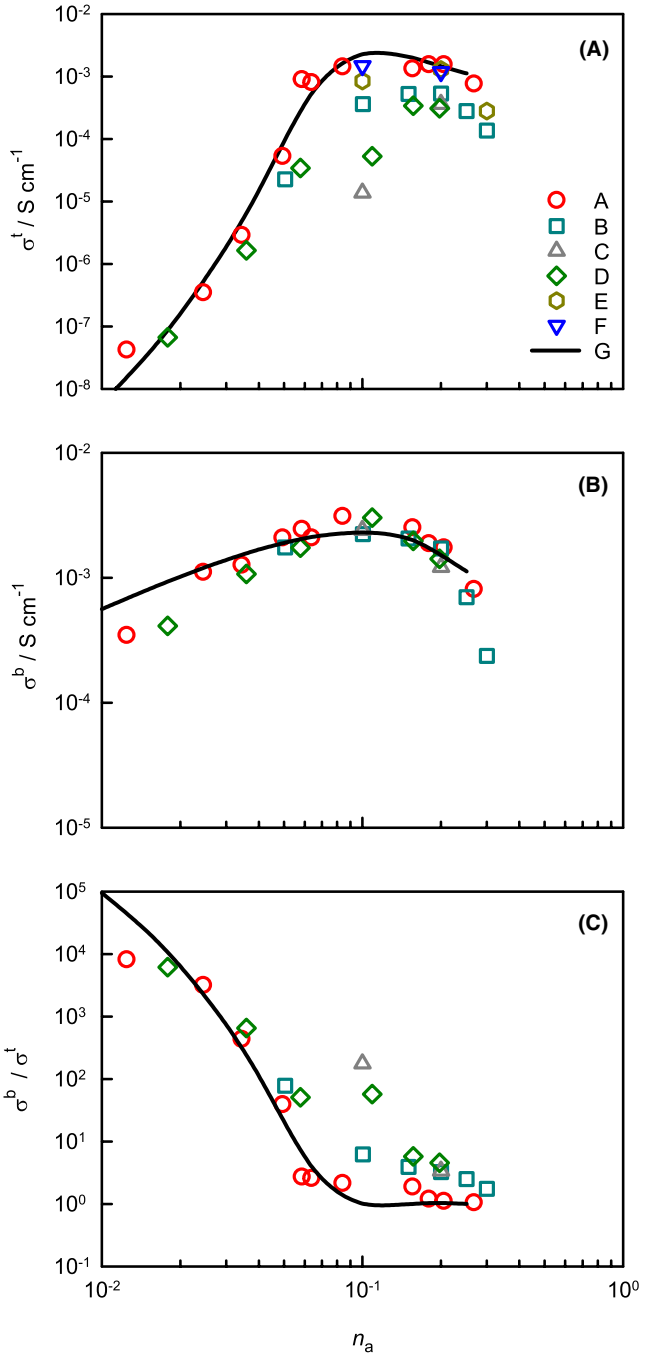

FIGURE 7 Conductivity σ of the CeO_2-Gd_2O_3 system as a function of Gd site fraction, n_a, at $T = 713$ K: (A) total conductivity σ^t, (B) bulk conductivity σ^b, (C) ratio σ^b/σ^t. Data taken from experiment and extrapolated or interpolated where necessary: (A) Tschöpe et al[5], (B) Tianshu et al[21], (C) Ralph et al[17], (D) Kim et al[31], (E) Kudo and Obayashi[108], (F) Kharton et al[50], (G) Calculated by combining Poisson-Cahn theory and the Nakayama-Martin model

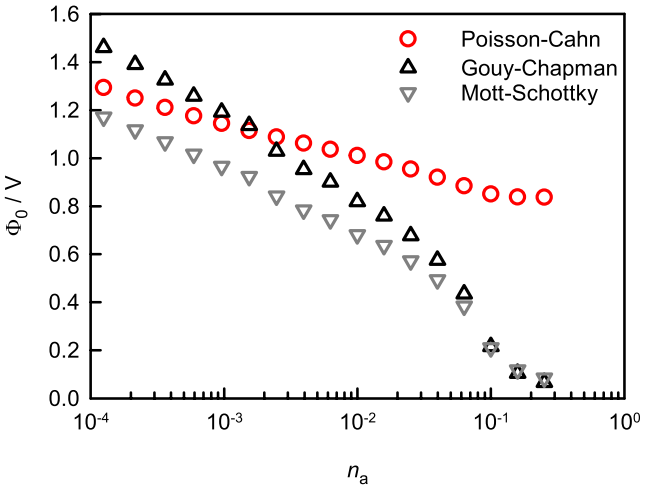

FIGURE 8 Comparison of the grain-boundary space-charge potential Φ_0 as a function of bulk acceptor site fraction n_a^b at $T = 713$ K in the CeO_2-Gd_2O_3 system. Poisson-Cahn values taken from the simulations. Gouy-Chapman and Mott-Schottky values obtained by analysing the Poisson-Cahn data of Figure 7C with Equations 11 and 17

two dilute-solution values, falling between them at the lowest n_a^b. This suggests that Equations 11 and 17, despite the three sources of discrepancy—neglecting restricted equilibrium; ignoring spatially varying mobility; including simplifying approximations—yield values of Φ_0 that reflect the space-charge potential at the interface. In the intermediate region, with site fractions from below one percent up to several percent, Φ_0^{GC} and Φ_0^{MS} diverge substantially from Φ_0^{PC}; and at high n_a^b, that is, above several percent, the dilute-solutions values bear no relation to the electrostatic potential at the interface. So, one can apply dilute-solution models to concentrated solid solutions, but the results one obtains will be meaningless.

Finally, we comment on other experimental procedures that can be used to extract the space-charge potential. One alternative electrical method, proposed by Kim and Lubomirsky, is the analysis of a polycrystal's current-voltage characteristics.[57] Such an analysis has been shown for ceria-based electrolytes to yield space-charge potentials different to those obtained by applying Equation 17 to conductivity data.[57,109] One consequence according to Kim and Lubomirsky is that there are additional sources of resistance (eg, a non-negligible core resistance[109]). It is not surprising, though, that the two approaches, current-voltage characteristics and resistance ratio, yield different values. Both approaches start by assuming incorrectly that the point defects in a concentrated solid solution behave as in a dilute solution, and then they take different routes to the space-charge potential. There is no reason to believe that they will yield the same value of Φ_0. It seems unnecessary, therefore, to invoke other sources of resistance, if the complexity of point-defect behavior in concentrated solid solution is not taken into account.

Consequently, there is a need to determine directly the space-charge potential at grain boundaries, and this can be

achieved by electron holography in a TEM or by scanning probe techniques. Conducting and analyzing such experiments is not trivial, however. In electron holography, large changes in composition (acceptor accumulation!) complicate the extraction of the electrostatic potential, while for scanning probe measurements, the grain-boundary potential has to be isolated from that arising from the surface space-charge layer.

5 | CONCLUDING REMARKS

The intrinsic simplicity of a dilute solution of point defects is beguiling, part of the allure being the ability to describe not only the bulk properties but also the interfacial properties of such a system with simple analytical expressions. Most oxide-ion conducting electrolytes, however, are concentrated solutions and thus constitute complex systems of point defects. The addition of interfaces that modify the complex point-defect behavior by generating deviations from local electroneutrality introduces yet further complexity. The application of dilute-solution concepts to systems that evidently do not conform to this degree of simplicity is, therefore, incorrect. In this study, we have concerned ourselves with some of the consequences.

We have demonstrated that there is no simple way to calculate the extent of the acceptor accumulation layers at a grain boundary in a concentrated solution. A characteristic screening length, analogous to the Debye length, can be derived from linearized Poisson-Cahn theory in a relatively simple fashion. It provides a means to determine quantitatively the (temperature-dependent) limit between dilute and concentrated solid solutions. But, owing to the linearization of a highly nonlinear problem, it fails to describe the extent of space-charge zones in concentrated solutions. The extent of the accumulation layer can only be obtained through solution of the Poisson-Cahn equations. In addition, we have demonstrated that there is no simple way to analyze the grain-boundary resistance of a concentrated solution. Worse still, the application of the standard analytical expressions from dilute-solution theories will generally yield values for the space-charge potential that, though not physically unreasonable, bear no relation to reality. In this way, we advocate the use of a sufficiently complex approach, such as Poisson-Cahn theory, to describe the complex electrical behavior of complex materials.

ACKNOWLEDGMENTS

X.T. and D.S.M. gratefully acknowledge funding from the National Science Foundation (CBET-1705397). R.A.D.S. gratefully acknowledges funding from German Research Foundation (DFG) within the Priority Program SPP 1959, "Manipulation of matter by electric and magnetic fields," (SO 499/9-1). Jana P. Parras is thanked for critical reading of the manuscript.

ORCID

David S. Mebane https://orcid.org/0000-0002-2198-7276

Roger A. De Souza https://orcid.org/0000-0001-7721-4128

REFERENCES

1. Poeppel RB, Blakely JM. Origin of equilibrium space charge potentials in ionic crystals. Surf Sci. 1969;15(3):507–23.
2. Bingham D, Tasker PW, Cormack AN. Simulated grain-boundary structures and ionic conductivity in tetragonal zirconia. Phil Mag A. 1989;60(1):1–14.
3. Jamnik J, Maier J, Pejovnik S. Interfaces in solid ionic conductors: equilibrium and small signal picture. Solid State Ionics. 1995;75:51–8.
4. Dabringhaus H, Butman MF. Theory of the Frenkel-Debye boundary layer at the (111) surface of pure CaF_2. J Phys: Condens Matter. 2003;15(34):5801–20.
5. Tschöpe A, Kilassonia S, Birringer R. The grain boundary effect in heavily doped cerium oxide. Solid State Ionics. 2004;173(1–4):57–61.
6. McIntyre PC. Equilibrium point defect and electronic carrier distributions near interfaces in acceptor-doped strontium titanate. J Am Ceram Soc. 2000;83(5):1129–36.
7. De Souza RA. The formation of equilibrium space-charge zones at grain boundaries in the perovskite oxide $SrTiO_3$. Phys Chem Chem Phys. 2009;11:9939–69.
8. Gregori G, Merkle R, Maier J. Ion conduction and redistribution at grain boundaries in oxide systems. Prog Mater Sci. 2017;89:252–305.
9. Dillon SJ, Tang M, Carter WC, Harmer MP. Complexion: a new concept for kinetic engineering in materials science. Acta Mater. 2007;55(18):6208–18.
10. Cantwell PR, Tang M, Dillon SJ, Luo J, Rohrer GS, Harmer MP. Grain boundary complexions. Acta Mater. 2014;62:1–48.
11. Wang DY, Nowick AS. The "grain-boundary effect" in doped ceria solid electrolytes. J Solid State Chem. 1980;35(3):325–33.
12. Adham KE, Hammou A. "Grain boundary effect" on ceria based solid solutions. Solid State Ionics. 1983;9-10:905–12.
13. Gerhardt R, Nowick AS. Grain-boundary effect in ceria doped with trivalent cations: I, electrical measurements. J Am Ceram Soc. 1986;69(9):641–6.
14. Balazs GB, Glass RS. AC impedance studies of rare earth oxide doped ceria. Solid State Ionics. 1995;76(1):155–62.
15. Christie GM, van Berkel F. Microstructure-ionic conductivity relationships in ceria-gadolinia electrolytes. Solid State Ionics. 1996;83(1–2):17–27.
16. Huang K, Feng M, Goodenough JB. Synthesis and electrical properties of dense $Ce_{0.9}Gd_{0.1}O_{1.95}$ ceramics. J Am Ceram Soc. 1998;81(2):357–62.
17. Ralph JM, Kilner JA, Steele B. Improving Gd-doped ceria electrolytes for low temperature solid oxide fuel cells. MRS Proc. 1999;575:309.

18. Lee JS, Kim DY. Space-charge concepts on grain boundary impedance of a high-purity yttria-stabilized tetragonal zirconia polycrystal. J Mater Res. 2001;16:2739–51.
19. Zhan Z, Wen TL, Tu H, Lu ZY. AC impedance investigation of samarium-doped ceria. J Electrochem Soc. 2001;148(5):A427–A432.
20. Tschöpe A, Sommer E, Birringer R. Grain size-dependent electrical conductivity of polycrystalline cerium oxide: I. Experiments. Solid State Ionics. 2001;139(3-4);255–65.
21. Tianshu Z, Hing P, Huang H, Kilner J. Ionic conductivity in the CeO_2–Gd_2O_3 system ($0.05 \leq Gd/Ce \leq 0.4$) prepared by oxalate coprecipitation. Solid State Ionics. 2002;148(3-4);567–73.
22. Zhou XD, Huebner W, Kosacki I, Anderson HU. Microstructure and grain-boundary effect on electrical properties of gadolinium-doped ceria. J Am Ceram Soc. 2002;85(7):1757–62.
23. Kim S, Maier J. On the conductivity mechanism of nanocrystalline ceria. J Electrochem Soc. 2002;149(10):J73–J83.
24. Guo X, Sigle W, Maier J. Blocking grain boundaries in yttria-doped and undoped ceria ceramics of high purity. J Am Ceram Soc. 2003;86(1):77–87.
25. Atkinson A, Baron SA, Brandon NP. AC impedance spectra arising from mixed ionic electronic solid electrolytes. J Electrochem Soc. 2004;151(5):E186–E193.
26. Guo X, Mi S, Waser R. Nonlinear electrical properties of grain boundaries in oxygen ion conductors: acceptor-doped ceria. Electrochem Solid-State Lett. 2005;8(1):J1–J3.
27. Jasinski P, Petrovsky V, Suzuki T, Anderson HU. Impedance studies of diffusion phenomena and ionic and electronic conductivity of cerium oxide. J Electrochem Soc. 2005;152(4):J27–J32.
28. Lai W, Haile SM. Impedance spectroscopy as a tool for chemical and electrochemical analysis of mixed conductors: a case study of ceria. J Am Ceram Soc. 2005;88(11):2979–97.
29. Guo X, Waser R. Electrical properties of the grain boundaries of oxygen ion conductors: acceptor-doped zirconia and ceria. Prog Mater Sci. 2006;51(2):151–210.
30. Kuharuangrong S. Ionic conductivity of Sm, Gd, Dy and Er-doped ceria. J Power Sources. 2007;171(2):506–10.
31. Avila-Paredes HJ, Choi K, Chen CT, Kim S. Dopant-concentration dependence of grain-boundary conductivity in ceria: a space-charge analysis. J Mater Chem. 2009;19:4837–42.
32. Lenka RK, Mahata T, Tyagi AK, Sinha PK. Influence of grain size on the bulk and grain boundary ion conduction behavior in gadolinia-doped ceria. Solid State Ionics. 2010;181(5):262–7.
33. Pérez-Coll D, Sánchez-López E, Mather GC. Influence of porosity on the bulk and grain-boundary electrical properties of Gd-doped ceria. Solid State Ionics. 2010;181(21):1033–42.
34. Sánchez-Bautista C. Dos Santos-García AJ, Peña-Martínez J, Canales-Vázquez J. The grain boundary effect on dysprosium doped ceria. Solid State Ionics. 2010;181(37):1665–73.
35. Yan D, Liu X, Bai X, Pei L, Zheng M, Zhu C, et al. Electrical properties of grain boundaries and size effects in samarium-doped ceria. J Power Sources. 2010;195(19):6486–90.
36. Lee KR, Lee JH, Yoo HI. Grain size effect on the electrical properties of nanocrystalline ceria. J Eur Ceram Soc. 2014;34(10):2363–70.
37. Zhang L, Liu F, Brinkman K, Reifsnider KL, Virkar AV. A study of gadolinia-doped ceria electrolyte by electrochemical impedance spectroscopy. J Power Sources. 2014;247:947–60.
38. Bowman WJ, Zhu J, Sharma R, Crozier PA. Electrical conductivity and grain boundary composition of Gd-doped and Gd/Pr co-doped ceria. Solid State Ionics. 2015;272:9–17.
39. Kazlauskas S, Kežionis A, Šalkus T, Orliukas AF. Effect of sintering temperature on electrical properties of gadolinium-doped ceria ceramics. J Mater Sci. 2015;50(8):3246–51.
40. Baral AK, Tsur Y. Impedance spectroscopy of Gd-doped ceria analyzed by genetic programming (ISGP) method. Solid State Ionics. 2017;304:145–9.
41. Baure G, Zhou H, Chung CC, Stozhkova MA, Jones JL, Nino JC. Grain orientation effects on the ionic conductivity of neodymia doped ceria thin films. Acta Mater. 2017;133:81–9.
42. Baure G, Zhou H, Chung CC, Buck MN, Stozhkova MA, Jones JL, et al. Comparison of the in- and across-plane ionic conductivity of highly oriented neodymium doped ceria thin films. Acta Mater. 2018;147:10–5.
43. Aidhy DS, Zhang Y, Weber WJ. Impact of segregation energetics on oxygen conductivity at ionic grain boundaries. J Mater Chem A. 2014;2:1704–9. https://doi.org/10.1039/C3TA14128D
44. Dholabhai PP, Aguiar JA, Wu L, Holesinger TG, Aoki T, Castro R, et al. Structure and segregation of dopant-defect complexes at grain boundaries in nanocrystalline doped ceria. Phys Chem Chem Phys. 2015;17:15375–85.
45. Arora G, Aidhy DS. Segregation and binding energetics at grain boundaries in fluorite oxides. J Mater Chem A. 2017;5:4026–35.
46. Tuller HL, Nowick AS. Doped ceria as a solid oxide electrolyte. J Electrochem Soc. 1975;122(2):255–9.
47. Eguchi K, Setoguchi T, Inoue T, Arai H. Electrical properties of ceria-based oxides and their application to solid oxide fuel cells. Solid State Ionics. 1992;52(1):165–72.
48. Inaba H, Tagawa H. Ceria-based solid electrolytes. Solid State Ionics. 1996;83(1):1–16.
49. Mogensen M, Sammes NM, Tompsett GA. Physical, chemical and electrochemical properties of pure and doped ceria. Solid State Ionics. 2000;129(1-4):63–94.
50. Kharton VV, Figueiredo FM, Navarro L, Naumovich EN, Kovalevsky AV, Yaremchenko AA, et al. Ceria-based materials for solid oxide fuel cells. J Mater Sci. 2001;36(5):1105–17.
51. Steele B. Appraisal of Ce1-yGdyO2-y/2 electrolytes for IT-SOFC operation at 500°C. Solid State Ionics. 2000;129(1–4):95–110.
52. Kilner JA, Burriel M. Materials for intermediate-temperature solid-oxide fuel cells. Ann Rev Mater Res. 2014;44(1):365–93.
53. Lee HB, Prinz FB, Cai W. Atomistic simulations of grain boundary segregation in nanocrystalline yttria-stabilized zirconia and gadolinia-doped ceria solid oxide electrolytes. Acta Mater. 2013;61(10):3872–87.
54. Yan PF, Mori T, Suzuki A, Wu YY, Auchterlonie GJ, Zou J, et al. Grain boundary's conductivity in heavily yttrium doped ceria. Solid State Ionics. 2012;222–223:31–7.
55. Yeh TC, Perry NH, Mason TO. Nanograin composite model studies of nanocrystalline gadolinia-doped ceria. J Am Ceram Soc. 2011;94(4):1073–8.
56. Tanaka R, Oliveira WS, Brandão A, Abrantes J, Frade JR. Grain boundary conductivity of heterogeneous ceria gadolinia. Electrochim Acta. 2012;85:116–21.
57. Kim SK, Khodorov S, Lubomirsky I, Kim S. A linear diffusion model for ion current across blocking grain boundaries in oxygen-ion and proton conductors. Phys Chem Chem Phys. 2014;16:14961–8.

58. Laethem DV, Deconinck J, Depla D, Hubin A. Finite element modelling of the ionic conductivity of acceptor doped ceria. J Eur Ceram Soc. 2016;36(8):1983–94.
59. Laethem DV, Deconinck J, Hubin A. Ionic conductivity of space charge layers in acceptor doped ceria. J Eur Ceram Soc. 2019;39:432–41.
60. Lei Y, Ito Y, Browning ND, Mazanec TJ. Segregation effects at grain boundaries in fluorite-structured ceramics. J Am Ceram Soc. 2002;85(9):2359–63.
61. Tian C, Chan SW. Ionic conductivities, sintering temperatures and microstructures of bulk ceramic CeO_2 doped with Y_2O_3. Solid State Ionics. 2000;134(1-2):89–102.
62. Jasper A, Kilner JA, McComb DW. TEM and impedance spectroscopy of doped ceria electrolytes. Solid State Ionics. 2008;179(2-26):904–8.
63. Li ZP, Mori T, Auchterlonie GJ, Zou J, Drennan J. Direct evidence of dopant segregation in Gd-doped ceria. Appl Phys Lett. 2011;98(9):093104.
64. Bowman WJ, Kelly MN, Rohrer GS, Hernandez CA, Crozier PA. Enhanced ionic conductivity in electroceramics by nanoscale enrichment of grain boundaries with high solute concentration. Nanoscale. 2017;9:17293–302.
65. Li F, Ohkubo T, Chen YM, Kodzuka M, Ye F, Ou DR, et al. Laser-assisted three-dimensional atom probe analysis of dopant distribution in Gd-doped CeO_2. Scr Mater. 2010;63(3):332–5.
66. Diercks DR, Tong J, Zhu H, Kee R, Baure G, Nino JC, et al. Three-dimensional quantification of composition and electrostatic potential at individual grain boundaries in doped ceria. J Mater Chem A. 2016;4:5167–75.
67. Dickey EC, Fan X, Pennycook SJ. Structure and chemistry of yttria-stabilized cubic-zirconia symmetric tilt grain boundaries. J Am Ceram Soc. 2001;84(6):1361–8.
68. Backhaus-Ricoult M, Badding M, Thibault Y. Grain boundary segregation and conductivity in yttria-stabilized zirconia. Ceram Trans. 2006;179:173–91.
69. Matsui K, Yoshida H, Ikuhara Y. Grain-boundary structure and microstructure development mechanism in 2–8 mol% yttria-stabilized zirconia polycrystals. Acta Mater. 2008;56(6):1315–25.
70. Feng B, Lugg NR, Kumamoto A, Ikuhara Y, Shibata N. Direct observation of oxygen vacancy distribution across yttria-stabilized zirconia grain boundaries. ACS Nano. 2017;11(11):11376–82. PMID: 29028310.
71. Ando K, Oishi Y. Diffusion characteristics of actinide oxides. J Nucl Sci Technol. 1983;20(12):973–82.
72. Kilo M, Taylor MA, Argirusis C, Borchardt G, Lesage B, Weber S, et al. Cation self-diffusion of ^{44}Ca, ^{88}Y, and ^{96}Zr in single-crystalline calcia- and yttria-doped zirconia. J Appl Phys. 2003;94(12):7547–52.
73. Kilo M, Jackson RA, Borchardt G. Computer modelling of ion migration in zirconia. Phil Mag. 2003;83(29):3309–25.
74. Beschnitt S, Zacherle T, De Souza RA. Computational study of cation diffusion in ceria. J Phys Chem C. 2015;119(49):27307–15.
75. Beschnitt S, De Souza RA. Impurity diffusion of Hf and Zr in Gd-doped CeO_2. Solid State Ionics. 2017;305(Supplement C):23–9.
76. Mebane DS, De Souza RA. A generalised space-charge theory for extended defects in oxygen-ion conducting electrolytes: from dilute to concentrated solid solutions. Energy Environ Sci. 2015;8:2935–40.
77. Cahn JW, Hilliard JE. Free energy of a nonuniform system. I. Interfacial free energy. J Chem Phys. 1958;28(2):258–67.
78. Cahn JW. Critical-point wetting. J Chem Phys. 1977;66(8):3667–72.
79. Mebane DS. A variational approach to surface cation segregation in mixed conducting perovskites. Comput Mater Sci. 2015;105:231–6.
80. Zurhelle AF, Tong X, Klein A, Mebane DS, De Souza RA. A space-charge treatment of the increased concentration of reactive species at the surface of a ceria solid solution. Angew Chem Int Ed. 2017;56:14516–20.
81. Denk I, Claus J, Maier J. Electrochemical investigations of $SrTiO_3$ boundaries. J Electrochem Soc. 1997;144(10):3526–36.
82. Kim S, Fleig J, Maier J. Space charge conduction: simple analytical solutions for ionic and mixed conductors and application to nanocrystalline ceria. Phys Chem Chem Phys. 2003;5:2268–73.
83. Göbel MC, Gregori G, Maier J. Numerical calculations of space charge layer effects in nanocrystalline ceria. Part I: comparison with the analytical models and derivation of improved analytical solutions. Phys Chem Chem Phys. 2014;16:10214–31.
84. Franceschetti DR. Local thermodynamic formalism for space charge in ionic crystals. Solid State Ionics. 1981;2(1):39–42.
85. Maier J. Ionic conduction in space charge regions. Prog Solid State Chem. 1995;23(3):171–263.
86. Jamnik J. Impedance spectroscopy of mixed conductors with semi-blocking boundaries. Solid State Ionics. 2003;157(1):19–28.
87. Maier J. Physical chemistry of ionic materials: ions and electrons in solids. Chichester, UK: John Wiley & Sons; 2004.
88. Ye F, Yin CY, Ou DR, Mori T. Relationship between lattice mismatch and ionic conduction of grain boundary in YSZ. Prog Nat Sci: Mater Int. 2014;24(1):83–6.
89. De Souza RA, Fleig J, Maier J, Zhang Z, Sigle W, Rühle M. Electrical resistance of low-angle tilt grain boundaries in acceptor-doped $SrTiO_3$ as a function of misorientation angle. J Appl Phys. 2005;97(5):053502.
90. Zhang Z, Sigle W, De Souza RA, Kurtz W, Maier J, Rühle M. Comparative studies of microstructure and impedance of small-angle symmetrical and asymmetrical grain boundaries in $SrTiO_3$. Acta Mater. 2005;53(19):5007–15.
91. Ramadan A, De Souza RA. Atomistic simulations of symmetrical low-angle [100] (01l) tilt boundaries in $SrTiO_3$. Acta Mater. 2016;118:286–95.
92. Rhoderick EH, Williams RH. Metal–semiconductor contacts. Oxford, UK: Clarendon Press; 1988.
93. De Souza RA, Munir ZA, Kim S, Martin M . Defect chemistry of grain boundaries in proton-conducting solid oxides. Solid State Ionics. 2011;196(1):1–8.
94. Grieshammer S, Grope B, Koettgen J, Martin M. A combined DFT + U and Monte Carlo study on rare earth doped ceria. Phys Chem Chem Phys. 2014;16:9974–86.
95. Žguns PA, Ruban AV, Skorodumova NV. Ordering and phase separation in Gd-doped ceria: a combined DFT, cluster expansion and Monte Carlo study. Phys Chem Chem Phys. 2017;19:26606–20.
96. Žuns PA, Ruban AV, Skorodumova NV. Phase diagram and oxygen-vacancy ordering in the CeO_2–Gd_2O_3 system: a theoretical study. Phys Chem Chem Phys. 2018;20:11805–18.
97. Koettgen J, Grieshammer S, Hein P, Grope B, Nakayama M, Martin M. Understanding the ionic conductivity maximum in doped ceria: trapping and blocking. Phys Chem Chem Phys. 2018;20:14291–321.

98. Puri S, Binder K. Surface-directed spinodal decomposition—phenomenology and numerical results. Phys Rev A. 1992;46(8):R4487–R4489.
99. Puri S, Binder K. Surface effects on spinodal decomposition in binary mixtures and the interplay with wetting phenomena. Phys Rev E. 1994;49:5359–77.
100. Lee HB, Prinz FB, Cai W. Atomistic simulations of surface segregation of defects in solid oxide electrolytes. Acta Mater. 2010;58(6):2197–206.
101. Gunn D, Purton JA, Metz S. Monte Carlo simulations of gadolinium doped ceria surfaces. Solid State Ionics. 2018;324:128–37.
102. Binder K, Frisch HL. Dynamics of surface enrichment: a theory based on the Kawasaki spin-exchange model in the presence of a wall. Z Phys B: Condens Matter. 1991;84(3):403–18.
103. Vikrant K, Chueh WC, Garcia RE. Charged interfaces: electrochemical and mechanical effects. Energy Environ Sci. 2018;11:1993–2000.
104. Sheldon BW, Shenoy VB. Space charge induced surface stresses: Implications in ceria and other ionic solids. Phys Rev Lett. 2011;106:216104.
105. Debye P, Hückel E. Zur Theorie der Elektrolyte. I. Gefrierpunktserniedrigung und verwandte Erscheinungen. Phys Z. 1923;24(9):185–206.
106. Bockris JO, Reddy A. Modern Electrochemistry: An Introduction to an Interdisciplinary Area. Vol. 1 of Modern Electrochemistry. New York, NY: Plenum Press; 1970.
107. Nakayama M, Martin M. First-principles study on defect chemistry and migration of oxide ions in ceria doped with rare-earth cations. Phys Chem Chem Phys. 2009;11:3241–9.
108. Kudo T, Obayashi H. Mixed electrical conduction in the fluorite-type $Ce_{1-x}Gd_xO_{2-x/2}$. J Electrochem Soc. 1976;123(3):415–9.
109. Kim S, Kim SK, Khodorov S, Maier J, Lubomirsky I. On determining the height of the potential barrier at grain boundaries in ion-conducting oxides. Phys Chem Chem Phys. 2016;18:3023–31.

AUTHOR BIOGRAPHIES

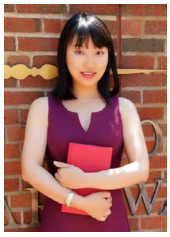

Xiaorui Tong obtained a B.S. in Mechanical Design, Manufacturing and Automation in 2011 and a M.S. in Mechanical Engineering at the Center for Intelligent Maintenance Systems (a NSF Industry/University Cooperative Research Center) in 2013. She worked with companies including the Goodyear Tire & Rubber Company and Parker Hannifin Corporation on developing computational models for various industrial systems. She received a Ph.D. in Material Science and Engineering from West Virginia University in 2018. Her work focuses on building sophisticated quantitative models using machine learning, big data analytics and physics-based approach for mechanical and material systems.

David S. Mebane is Associate Professor of Mechanical and Aerospace Engineering and leader of the Energy Systems and Materials Simulation Group at West Virginia University. He received a Ph.D. in Materials Science and Engineering from Georgia Tech and held postdoctoral positions at the Max Planck Institute for Solid State Research and the National Energy Technology Laboratory. His work focuses on the integration of sophisticated scientific understanding of materials into system and process-scale models.

Roger A. De Souza obtained a B. Eng. in Material Science and Engineering in 1992 and a Ph.D. in Materials Science in 1996 from Imperial College London. After spending two years as a post-doctoral researcher at Karlsruhe University, he moved to the Max Planck Institute for Solid State Research in Stuttgart. In 2002 he joined the Institute of Physical Chemistry at RWTH Aachen University, where he received his professorial degree (Habilitation) in 2011 and was promoted to Professor in 2017. The De Souza group performs fundamental research, encompassing both experimental and computational approaches, on complex oxides for energy and information technologies.

How to cite this article: Tong X, Mebane DS, De Souza RA. Analyzing the grain-boundary resistance of oxide-ion conducting electrolytes: Poisson-Cahn vs Poisson-Boltzmann theories. *J Am Ceram Soc*. 2020;103:5–22. https://doi.org/10.1111/jace.16716